ACS Chemical Neuroscience
Cite This: ACS Chem. Neurosci. 2019, 10, 2467−2480
Research Article
pubs.acs.org/chemneuro

How Does Chirality Determine the Selective Inhibition of Histone Deacetylase 6? A Lesson from Trichostatin A Enantiomers Based on Molecular Dynamics

Yang Zhang,[§,†] Jun Biao Ying,[§] Jia Jun Hong,[§] Feng Cheng Li,[§] Ting Ting Fu,[†] Feng Yuan Yang,[†] Guo Xun Zheng,[†] Xiao Jun Yao,[‡] Yan Lou,[€] Yunqing Qiu,[€] Wei Wei Xue,*[,†] and Feng Zhu*[,§,†]

[§]Lab of Innovative Drug Research and Bioinformatics, College of Pharmaceutical Sciences, Zhejiang University, Hangzhou 310058, China

[†]Innovative Drug Research and Bioinformatics Group, School of Pharmaceutical Sciences and Collaborative Innovation Center for Brain Science, Chongqing University, Chongqing 401331, China

[‡]State Key Laboratory of Applied Organic Chemistry and Department of Chemistry, Lanzhou University, Lanzhou 730000, China

[€]Zhejiang Provincial Key Laboratory for Drug Clinical Research and Evaluation, The First Affiliated Hospital, Zhejiang University, Hangzhou 310000, China

Supporting Information

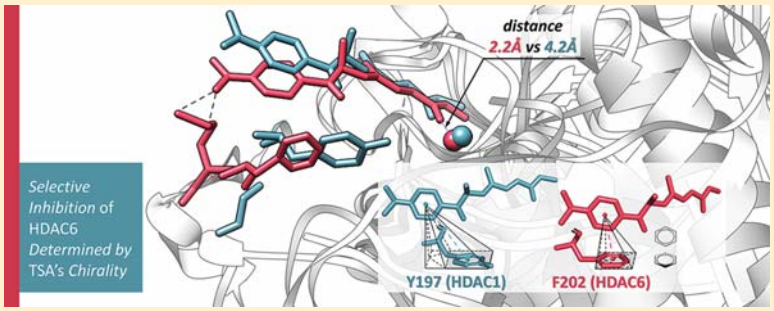

ABSTRACT: Histone deacetylase 6 (HDAC6) plays a key role in a variety of neurological disorders, which makes it attractive drug target for the treatment of Alzheimer's disease, Parkinson's disease, and memory/learning impairment. The selectivity of HDAC6 inhibitors (sHDAC6Is) are widely considered to be susceptible to the sizes of their Cap group and the physicochemical properties of their linker or zinc-binding group, which makes the discovery of new sHDAC6Is extremely difficult. With the discovery of the distinct selectivity between Trichostatin A (TSA) enantiomers, the chirality residing in the connective units between TSA's Cap and linker shows a great impact on its selectivity. However, the mechanism underlining (*S*)-TSA's selectivity is still elusive, and the way chirality switches the selective (*S*)-TSA to nonselective (*R*)-TSA is unknown. In this study, multiple computational approaches were collectively applied to explore, validate, and differentiate the binding modes of two TSA enantiomers in HDACs (especially the HDAC6) at atomic level. First, two nonconservative residues (G200/M205 and Y197/F202 in HDAC1/6) in loop3 and four conservative residues deep inside the hydrophobic binding pocket were discovered as the decisive residues of (*S*)-TSA's selectivity toward HDAC6. Then, a novel mechanism underlying the selectivity of (*S*)-TSA toward HDAC6 was proposed, which was composed of the trigger by two nonconservative residues F202 and M205 in HDAC6 and a subsequently improved fit of (*S*)-TSA deep inside HDAC6's hydrophobic binding pocket. TSA enantiomers were used as a molecular probe to explore the mechanism underlying sHDAC6Is' selectivity in this study. Because of their decisive roles in (*S*)-TSA's selectivity to HDAC6, both F202 and M205 in HDAC6 should be especially considered in the discovery of novel sHDAC6Is.

KEYWORDS: *Selective HDAC6 inhibitor, neurodegenerative disease, Trichostatin A, chirality, molecular dynamics*

INTRODUCTION

The abnormal variations in epigenetics change the expression of disease genes and therefore contribute significantly to the development of numerous disorders, especially several neurodegenerative disorders and a variety of cancers.[1−7] As one of the fundamental mechanisms mediating the epigenetic phenomena, the histone modification by the cell is capable of balancing the activity of histone deacetylase (HDAC) and histone acetyltransferase (HAT) to promote removal and addition of acetyl groups from the tails of lysine in

Received: December 24, 2018
Accepted: February 20, 2019
Published: February 20, 2019

DOI: 10.1021/acschemneuro.8b00729
ACS Chem. Neurosci. 2019, 10, 2467−2480

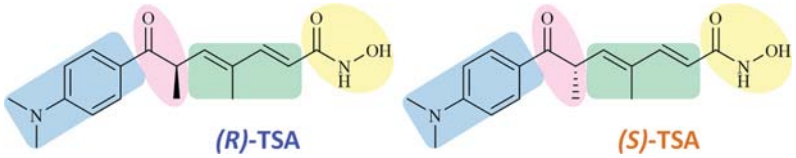

Figure 1. Chemical structure of (*R*)- and (*S*)-TSA. The capping group (Cap), the connect unit (CU), the linker, and the Zn^{2+} chelator (ZBG) regions are colored by blue, pink, green, and yellow backgrounds, respectively.

histones.[8−11] In most cases, the histone deacetylation represses transcription, while histone acetylation plays the opposite role.[12] So far, the attention has been mainly focused on HDAC, because it plays the key role in reversing aberrant epigenetic change relating to the neurological and inflammatory pathologies.[13] The suppression of HDACs leads to the gradual increase of acetylated histone and brings about various cell-dependent responses including cell death/differentiation, cardiac functions, neuroplasticity, and so on.[9,14] Thus, HDAC inhibitors (HDACi) show a great therapeutic potential in the treatment of various diseases associated with aberrant cellular proliferation.[15−20]

Among the proteins in the HDAC family, the HDAC6 is unique in its structure and function[21,22] and is the only isozyme containing two catalytic domains (CD1 and CD2). CD2 is found to be responsible for the main catalytic activity exhibiting broad substrate specificity[23] and is able to catalyze the deacetylation of K40 of α-tubulin in the lumen of microtubule.[24] So far, HDAC6 has been identified as playing a key role in stress adaption,[25−29] the development of Alzheimer's disease,[30] and post-transcriptional regulation of proteins in brain.[31] Severe adverse effects are frequently reported in the clinical applications of broad-spectrum HDAC inhibitors,[32−36] which are attributed to the complicated physiological effects induced by multiple HDAC subtypes.[32] Thus, the selective inhibition of HDAC6 is proposed as a novel strategy to minimize drug toxicity and limit off-target collateral effects.[34] Especially for treating neurodegenerative diseases, several studies reported that the selective inhibition of HDAC6 can not only achieve enhanced therapeutic effects but also minimize the adverse effects frequently encountered in the treatments based on pan-HDAC inhibitors.[37−43]

So far, extensive efforts have been made to develop the selective inhibitor of HDAC6 (sHDAC6I), and a number of sHDAC6Is have been discovered such as Tubastatin,[37] Nexturastat A,[38] Ricolinostat,[39] and HPOB.[40] On the basis of the pharmacophore models of the first FDA-approved pan-HDAC inhibitor-SAHA, the structures of HDAC inhibitors can be generally divided into four components: a capping group (Cap), a connect unit (CU), a zinc-binding group (ZBG), and a linker between CU and ZBG (linker). The Cap can interact with the rim of the catalytic tunnel of HDACs, the linker can enhance the binding affinity through its contacts with the residues within the drug-binding pocket, the CU region links the Cap with linker, and ZBG chelates the zinc ion at the bottom of the drug-binding pocket and competes with the catalytic center for the zinc ion. As shown in Supplementary Figure S1, the structure of these inhibitors conforms to that of traditional pan-HDAC inhibitors. In particular, the structures of these inhibitors are composed of four components: a capping group (Cap), a connect unit (CU), a linker, and a Zn^{2+} chelator (ZBG).[41]

Previous studies reported that the Cap and linker groups played vital roles in determining the selective inhibitory activities of HDAC inhibitors, and generally, the HDAC6 selective inhibitors are thought to be determined by the bulky Cap or linker group.[37,38,42] The CU region is reported to be frequently modified by adding chain alkane substituents or hydroxyethyl groups (like Nexturastat A and HPOB), which largely enhances the ligands' selectivity toward HDAC6.[38,40] For the linker group of HDAC inhibitors, the unsaturated- or saturated-chain hydrocarbons are reported to be replaced by the aromatic rings, which contribute to the hydrophobic interactions between linker and active pocket.[43] The modification of the ZBG region (like hydroxamic group, sulfonamide group, sulfydryl, etc.) can also enhance the selectivity of the inhibitor to some extent.[43] However, an enlarged Cap was reported to generally increase inhibitors' lipophilicity, which, as a result, made them less druggable;[21,37,44] an enlarged linker resulted in the increase of molecular mass, which could reduce the ligand efficiency of studied inhibitor;[45] sulfur-containing ZBG-based HDAC6 inhibitors were found to generally show weak cellular activity.[46] Thus, the difference in the design strategies of molecular modifications results in huge variation in molecular skeletons (shown in Supplementary Figure S1),[37−40,47−49] and there are both advantages and disadvantages among current strategies, which reflects the tremendous difficulty in the discovery of novel sHDAC6I and requires the discovery of a new strategy for the design of this kind of molecule.

Recently, the Trichostatin A (TSA) enantiomers (Figure 1) with distinct profiles of HDAC6 selectivity arouse great interest.[50,51] In particular, the *R*-stereoisomer of TSA is found to be a strong dual inhibitor of both HDAC6 (IC_{50} = 4.8 nM) and HDAC1 (IC_{50} = 5.8 nM),[50,52] whereas the unnatural enantiomer (*S*)-TSA is found to be extremely selective to HDAC6 (~20-fold activity compared with HDAC1).[50] Considering the extensive complexity and tremendous difficulty in discovering novel sHDAC6Is based on the direct modifications on the Cap, CU, linker , or ZBG, it is of great interest to explore the mechanism underlying the distinct selectivity profile induced by simply "switching" the inhibitor chirality. In other words, as a result of the extreme simplicity and highly controllable nature of enantiomers, the discovery of the differential binding mechanism between (*R*)- and (*S*)-enantiomers may offer great insights into the rational design of new sHDAC6I. However, the target-binding mechanism underlining (*S*)-TSA's selectivity is still elusive, and the way chirality switches the selective (*S*) to nonselective (*R*) is largely unknown.

Herein, a variety of in silico approaches were combined to explore, validate, and distinguish the binding mechanisms of TSA enantiomers in both HDAC1 and HDAC6 at the atomic level. First, the studied systems of HDAC1/HDAC6 complexed with (*R*)/(*S*)-TSA were constructed, and the binding modes of (*R*)/(*S*)-TSA in HDAC1/HDAC6 were discovered. Second, the resulting models of MD simulation were verified, and the hot/warm-spot residues for target−

DOI: 10.1021/acschemneuro.8b00729
ACS Chem. Neurosci. 2019, 10, 2467−2480

ligand interaction were identified. Finally, the effects of TSA's chirality on target binding were analyzed and the key residues contributing to (*S*)-TSA's selectivity to HDAC6 were discovered. In summary, the mechanism underlining (*S*)-TSA's selectivity and how TSA's chirality switched this selectivity was revealed by differential energy contributions among key residues, which may facilitate sHDAC6I-based novel drug discovery in the future.

RESULTS AND DISCUSSION

Constructing the Studied Systems of HDAC1/HDAC6 Complexed with (*R*)/(*S*)-TSA. On the basis of the crystal structures of HDAC1 and HDAC6 in the *Protein Data Bank*,[23,60] the molecular docking was conducted to dictate the starting conformations of (*R*)- and (*S*)-TSA within HDAC1 and HDAC6, and the docking score and the level of similarity to the original conformations of ligands in the X-ray crystals have been considered. Docking results could be superimposed into the resolved crystal structures (5EDU,[23] 5ICN,[60] 5G0H,[50] and 1T64[97]) available in the *Protein Data Bank*, which could be used as references for determining the initial structures. As shown in Figure 2, the binding site of (*R*)- and

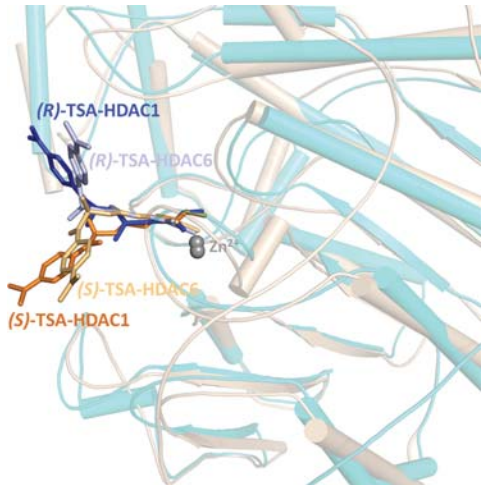

Figure 2. Structural superimposition of the initial docking conformations of (*R*)/(*S*)-TSA in HDAC1 (wheat) and HDAC6 (cyan). Particularly, (*R*)-TSA in HDAC1, (*R*)-TSA in HDAC6, (*S*)-TSA in HDAC1, and (*S*)-TSA in HDAC6 are colored in blue, light blue, orange, and light orange, respectively.

(*S*)-TSA in HDAC1/HDAC6 was mainly composed of flexible loops, and the Cap groups of (*R*)- and (*S*)-TSA were oriented toward different loop areas. Moreover, cross-docking and crystallized poses of TSA (4QA3[98] and 5G0H[50]) were subsequently aligned to evaluate the accuracy and effectiveness of the applied method. The consistency between these conformations (Supplementary Figure S2) denoted that the docking approach adopted in this research could produce poses that were in good agreement with the crystal structures.

Evaluating the Simulation Stability by Root-Mean-Square Deviation Analysis. The initial complexes of TSA–HDAC ((*R*)-TSA–HDAC6, (*S*)-TSA–HDAC6, (*R*)-TSA–HDAC1, and (*S*)-TSA–HDAC1) obtained from docking results were first assessed by a 500 ns simulation for achieving equilibrium. The dynamic stabilities of four studied systems were monitored by structural root-mean-square deviation (RMSD) of the backbone atoms of HDAC, heavy atoms of TSA, and atoms of the residues in the active site (within 2 Å of TSA), which fluctuated with the flow of time. On the basis of the RMSD assessment (Figure 3), all systems could reach the state of equilibrium around 150 ns with slight variation. Furthermore, all dynamic simulations were extended by additional 350 ns calculations, which demonstrated a continuous and stable equilibration in all four systems. The structural shifts between the equilibrated simulation results and the corresponding docking poses for all four systems are provided in Supplementary Figure S3.

Verifying the Resulting Models of MD Simulation Based on Experimental Data. The binding free energies (BFEs) of these four systems ((*R*)-TSA–HDAC6, (*R*)-TSA–HDAC1, (*S*)-TSA–HDAC6, and (*S*)-TSA–HDAC1) were calculated using the MM/GBSA approach, and the results were −41.83, −40.74, −38.91, and −33.19 kcal/mol, respectively. Additionally, the BFEs of all four systems were further theoretically inferred from previous experimental reports.[50] Particularly, the IC_{50} values from experiment[50] could be used to deduce the binding energy based on the following formula $\Delta G_{exp} = RT\ln(IC_{50})$, and the resulting binding energies (as shown in Table 1) were −11.80, −11.68, −11.27, and −9.48, respectively. As reported, the variations between the calculated BFE ($\Delta\Delta G$) of a complex and a reference (in this case, (*R*)-TSA–HDAC6) could effectively measure the level of experimental results successfully reproduced by the theoretical simulations.[77,84] Thus, the correlation between the simulation of this study ($\Delta\Delta G_{MM/GBSA}$) and the experimental results ($\Delta\Delta G_{exp}$) was analyzed. As demonstrated in Table 1, the relative BFEs of (*R*)-TSA–HDAC6, (*R*)-TSA–HDAC1, (*S*)-TSA–HDAC6, and (*S*)-TSA–HDAC1 simulated in this study ($\Delta\Delta G_{MM/GBSA}$) equaled 0, 1.09, 2.92, and 8.64 kcal/mol, which followed the same ascending trend as that from experiment ($\Delta\Delta G_{exp}$, from 0 to 0.12 to 0.53 to 2.32), but the simulation results were found to be slightly higher than those of the experiment. As reported by previous studies, it is unnecessary to consider the energy contribution of entropy when assessing the affinity order of binding ligands with similar binding poses and structures.[78,92,99] The above-mentioned higher estimation by simulation was reported to be inevitable with the application of the MM/GBSA approach.[100−104] In summary, the ascending trend of the experiment-based energy differences ($\Delta\Delta G_{exp}$) was reproduced very well by the simulation in this study ($\Delta\Delta G_{MM/GBSA}$), which could serve as the first evidence verifying the model constructed using the simulation here. Moreover, the calculation results of each subenergy term were provided in Table 2. In particular, ΔE_{vdw} and ΔE_{ele} were discovered as the main components contributing to TSA's binding, and the energy of polar-solvent (ΔG_{pol}) was found to hamper the binding of TSA to HDAC.

Besides the consistent trend of the relative binding free energy between simulation and experiments described in the above paragraph, another proof relied on crystallography studies reporting the crystallized structures of (*R*)- and (*S*)-TSA with *Danio rerio* HDAC6 CD2[50] and (*R*)-TSA with human HDAC8.[98] In particular, the structures of *Danio rerio* HDAC6 CD2 in complex with (*S*)-TSA (5G0H[50]) and (*R*)-TSA (5WGI[50]) were used as the reference to verify the simulation model constructed in this study by aligning them with the representative snapshot obtained from the equilibrated simulation trajectories. Meanwhile, the structure of

DOI: 10.1021/acschemneuro.8b00729
ACS Chem. Neurosci. 2019, 10, 2467−2480

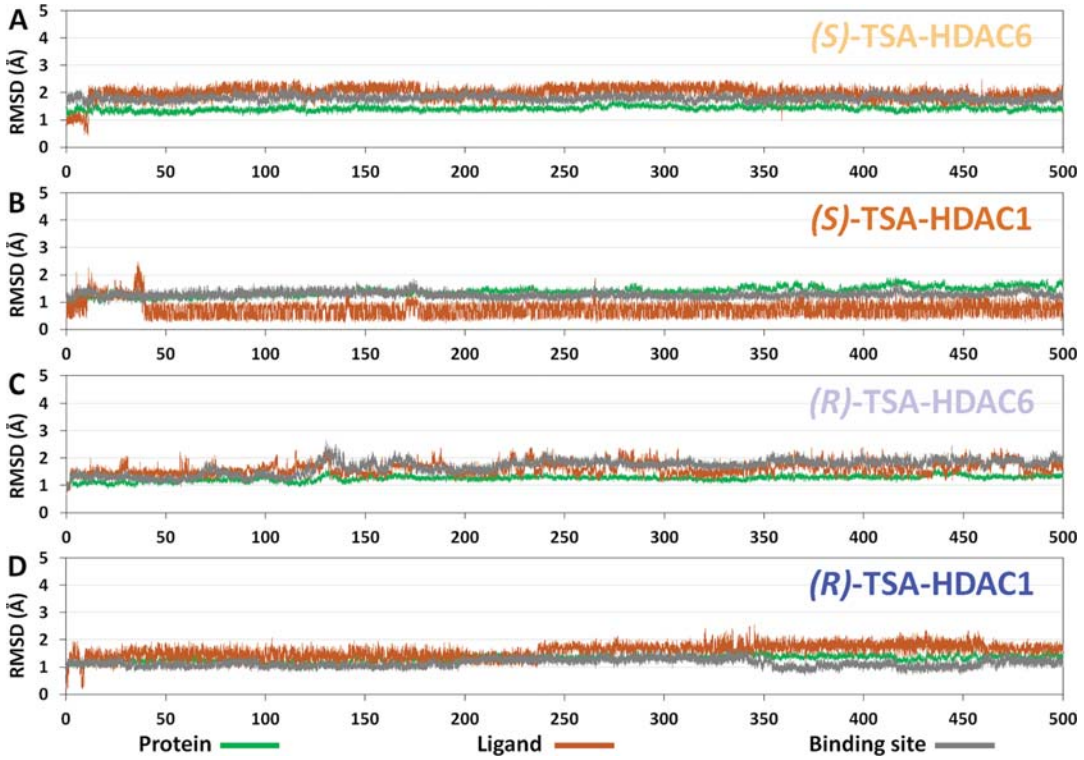

Figure 3. Root-mean-square deviations of protein backbone atoms, ligand heavy atoms, and binding site residue backbone atoms as a function of time in MD simulations.

Table 1. Calculated and Experimental Data of (*R*)/(*S*)-TSA Binding to HDAC1 and HDAC6[a]

systems	IC_{50}[b]	ΔG_{exp}[c]	$\Delta\Delta G_{exp}$[d]	$\Delta G_{MM/GMBA}$[e]	$\Delta\Delta G_{MM/GMBA}$[d]
(*R*)-TSA–HDAC6	4.76	−11.80	0.00	−41.83	0.00
(*R*)-TSA–HDAC1	5.76	−11.68	0.12	−40.74	1.09
(*S*)-TSA–HDAC6	11.1	−11.27	0.53	−38.91	2.92
(*S*)-TSA–HDAC1	206	−9.48	2.32	−33.19	8.64

[a]ΔG is in kcal/mol, and IC_{50} value is in nM. [b]IC_{50} values obtained from previous study.[50] [c]Estimated binding affinities based on IC_{50} values by the equation $\Delta G_{exp} = RT\ln(IC_{50})$, where R = 8.314 J/(mol·K), and T = 310.0 K. [d]$\Delta\Delta G$ is defined as the change of binding free energy using (*R*)-TSA–HDAC6 as a reference. [e]Calculated MM/GBSA binding free energies in this study.

Table 2. Detailed Energy Terms Calculated by MD Simulation in This Study[a]

systems	ΔE_{ele}	ΔE_{vdW}	ΔG_{nonpol}	ΔG_{pol}
(*R*)-TSA–HDAC6	−34.49	−30.20	−4.84	27.70
(*R*)-TSA–HDAC1	−31.20	−31.92	−4.85	27.24
(*S*)-TSA–HDAC6	−38.02	−27.08	−4.43	26.18
(*S*)-TSA–HDAC1	−22.31	−33.38	−4.63	27.13

[a]ΔG is in kcal/mol.

human HDAC8 (belonging to the same HDAC class as HDAC1) in complex with (*R*)-TSA (4QA3[98]) was used to validate the simulation models for HDAC1. As shown in Supplementary Figure S4A,B, the orientations of (*R*)/(*S*)-TSA along the ligand-binding pockets of crystal *Danio rerio* HDAC6 CD2 and simulated TSA–HDAC6 complexes were consistent. In other words, the simulation result of TSA–HDAC6 maintained a binding mode similar to crystal structures.[50] Moreover, as shown in Supplementary Figure S4C, the orientation of (*R*)-TSA in HDAC8[98] was consistent with that of the simulated (*R*)-TSA–HDAC6 complex.

Identification of the Hot- and Warm-Spot Residues for Target–Ligand Interaction. The HDACs belong to the metalloprotein family, and the zinc ion plays important roles for maintaining the biocatalytic activity of HDACs. HDAC inhibitors exert inhibitory activities mainly by competing with HDACs' catalytic centers for zinc ions; it is thus necessary to consider the chelation strength of the ZBG region with zinc ion. Herein, all complexes were processed based on the nonbonded model (126-4 LJ-type) conjugating with a SPC/E water model,[74,75] which explicitly considered the charge-induced dipole interaction.[74] In order to discover the important residues (hot- and warm-spots) contributing to TSA–HDAC interactions, amino acids with a high contribution of energy (≥0.1 kcal/mol) to the interaction in no less than one complex were discovered, which resulted in a total of 29 amino acids. As shown in Figure 4, the per-residue energy contributions of various amino acids in each complex varied significantly (taking (*S*)-TSA–HDAC1 as example, the contribution of Phe198 equaled −3.07 kcal/mol, which is almost 12 times that of Leu132's contribution). Moreover, the per-residue contributions of the same residue in various systems varied greatly (taking Leu272 in HDAC6/Leu264 in HDAC1 as example, it contributed −0.14, −0.99, −2.04, and −2.40 kcal/mol to the binding of (*S*)-TSA–HDAC6, (*S*)-TSA–HDAC1, (*R*)-TSA–HDAC1, and (*R*)-TSA–HDAC6, respectively). Moreover, the zinc ion in each complex was

DOI: 10.1021/acschemneuro.8b00729
ACS Chem. Neurosci. 2019, 10, 2467–2480

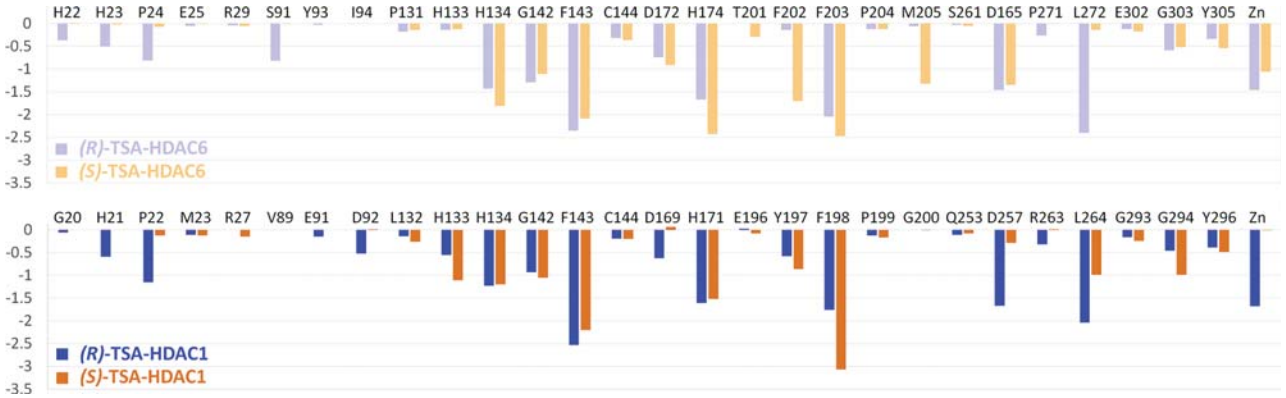

Figure 4. Per-residue binding free energy decomposition of 29 residues with high energy contribution (≥0.1 kcal/mol) to the interaction in at least one studied complex: (*R*)-TSA−HDAC6, (*S*)-TSA−HDAC6, (*R*)-TSA−HDAC1, and (*S*)-TSA−HDAC1.

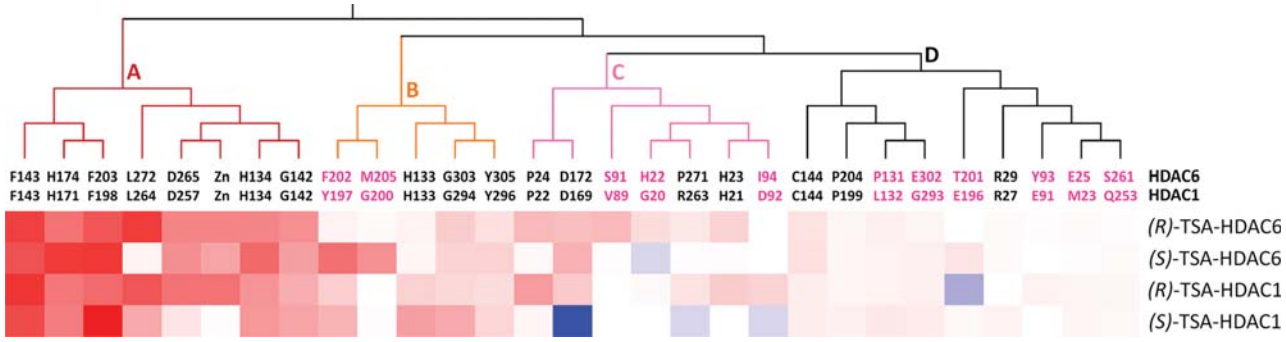

Figure 5. Identification of the hot- and warm-spot residues by hierarchically clustering per-residue energy contributions across four systems. The residues with high contribution (≥0.1 kcal/mol) to the interaction in at least one complex were partitioned into four groups (**A**, **B**, **C**, and **D**). Residues favoring the binding of TSA are colored in red (the residue with the highest contribution was colored in exact red, and the lower contribution residue was set to fade gradually to white). Residues hampering the binding of TSA are displayed in blue (the residue interfering with binding the most was colored as standard blue, and the residue interfering with binding the least was set to fade gradually to white). The white color here denotes residue with no contribution to TSA's binding.

processed by the 126-4 model,[69] and its energy contribution was calculated and provided in Figure 4 (represented by Zn). For all four studied systems, the energy contribution of the zinc ion also varied significantly.

The hierarchical clustering[105] of per-residue energy contribution across four systems was further applied to identify the hot- and warm-spot residues. As illustrated in Figure 5, the amino acids with a high contribution of energy (≥0.1 kcal/mol) in no less than one complex were partitioned to four groups (**A**, **B**, **C**, and **D**). The amino acid of the largest energy contribution (−3.07 kcal/mol) was shown in exact red, and the lower contributions faded toward white (without any energy). The amino acid causing the most energy hampering of the binding (0.02 kcal/mol) was shown in exact blue color, and the rest of the negative contributions reduced toward white (without any energy). On the basis of the clustered residues in Figure 5, the contributions of the residues in group **A** were found to be "consistently strong" across all complexes (hot spot), which accounted for 71.3, 66.1, 68.4, and 68.3% of the total contribution of all 29 residues in Figure 5 to the binding of complexes (*R*)-TSA−HDAC6, (*S*)-TSA−HDAC6, (*R*)-TSA−HDAC1, and (*S*)-TSA−HDAC1, respectively, which demonstrated the key role of these residues in the binding. Moreover, the residues in groups **B** and **C** were found to be warm spot with "relatively strong" contribution in four complexes, and their energy contributions account for 24.2, 27.6, 26.7, and 23.1% of the contribution of all 29 residues to the binding of (*R*)-TSA−HDAC6, (*S*)-TSA−HDAC6, (*R*)-TSA−HDAC1, and (*S*)-TSA−HDAC1, respectively. Compared to hot-spot residues, the warm-spot residues might not be necessarily conserved (residues colored in pink shown in Figure 5), but may regulate ligand affinity to target and thus affect their selectivity.[106]

To further elaborate the three-dimensional distribution of the 8 hot-spot residues (including Zn) and 12 warm-spot residues, a schematic diagram showing the interaction between TSA and residues is provided in Figure 6. As illustrated, the HDAC-binding site was composed of seven loop (L) domains with four loops (L5−L7 and a part of L4) constituting the active pocket and another four loops (L1−L3 and part of L4) surrounding the active pocket. The hot-spot residues in group **A** were colored in red and were primarily located in the active pocket. The warm-spot residues were colored in orange and pink and primarily lied in those surrounding loops and the region deep inside the active pocket (L6 and L7).

Effect of TSA's Chirality on Its Binding to HDAC1/HDAC6. To identify the effect of TSA's chirality on its binding to HDAC, the per-residue energy contribution of all hot- and warm-spot residues is shown in Figure 7, and the significant per-residue energy variations of given residues between any two complexes were highlighted by stars (four- or five-point stars). The 20 hot- and warm-spot residues in Figure 7 were

DOI: 10.1021/acschemneuro.8b00729
ACS Chem. Neurosci. 2019, 10, 2467−2480

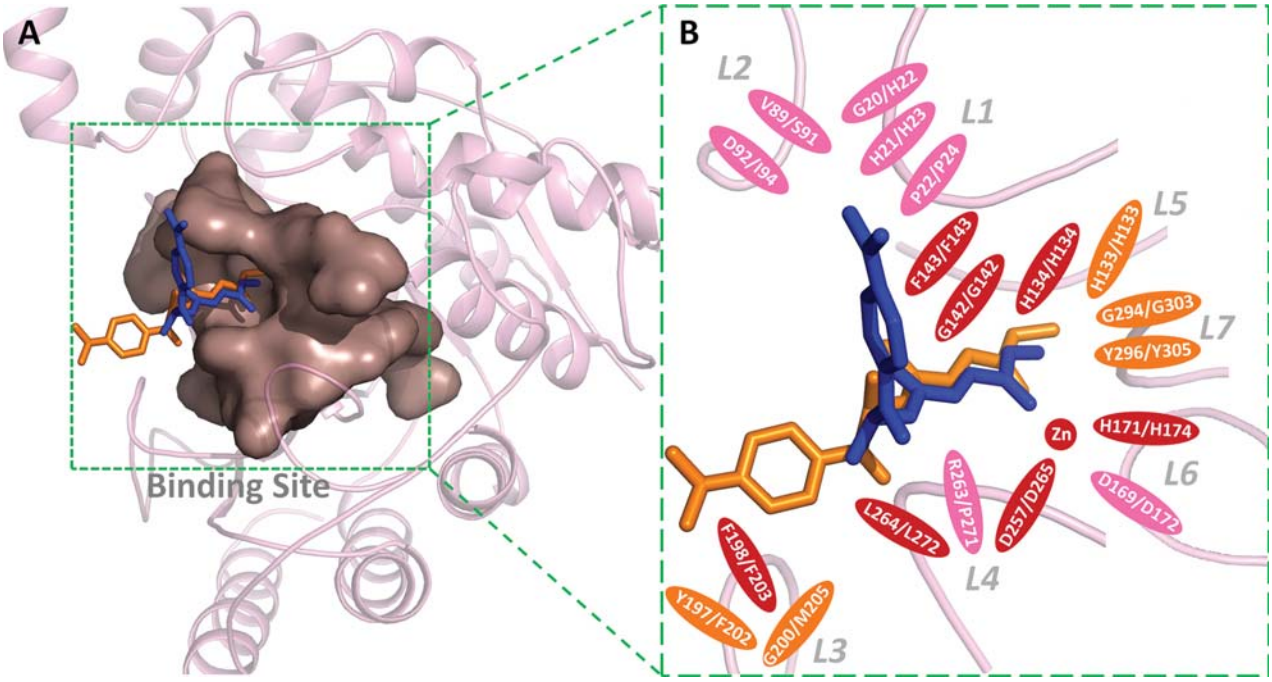

Figure 6. Schematic representation of the three-dimensional distribution of those 29 residues with high energy contribution (≥0.1 kcal/mol) to the interaction in at least one studied complex. The hot-spot residues in group **A** of Figure 5 are colored in red and primarily located in the active pocket. Those warm-spot residues in groups **B** and **C** of Figure 5 are colored in orange and pink and primarily lay in those surrounding loops and the region deep inside the active pocket (L6 and L7).

ordered according to their three-dimensional distribution (from loop L1 to L7). As shown in Figure 7A, the per-residue energy contributions of hot- and warm-spot residues in two complexes of (*R*)-TSA−HDAC1 and (*S*)-TSA−HDAC1 were provided, and the residues of significantly higher or lower energy contributions (≥0.5 kcal/mol) in (*R*)-TSA−HDAC1 as compared to (*S*)-TSA−HDAC1 were highlighted by a blue five-point star or orange four-point star, respectively. As a result, there were seven residues (H21, P22, D92, D257, L264, and D169, together with Zn) in HDAC1 that were highlighted by blue five-point star, and only three residues (F198, H133, and G294) were highlighted by the orange four-point star. These results demonstrated the key role of the six residues and Zn in determining the substantially higher affinity of (*R*)-TSA in HDAC1 than that of (*S*)-TSA. Moreover, those 6 + 3 residues and Zn of significant per-residue energy variations (indicated by star in Figure 7A) were further highlighted in the TSA−HDAC1-binding structure revealed by MD simulation (Figure 8). As illustrated, the Cap groups of (*R*)-TSA and (*S*)-TSA oriented to different loop domains because of the chirality residing in the CU group, which led to a difference in energy contribution of the same residue. Among the residues beneficial for (*R*)-TSA's binding, there were two hot-spot residues (D257 and L264 located in loop L4) and four warm-spot residues (H21 and P22 in loop L1, D92 in loop L2, and D169 in loop L6). Compared to the (*R*)-TSA−HDAC1, only three residues with the significant energy contribution variation for (*S*)-TSA's binding in HDAC1 were identified, which may be the reason for its reduced affinity.

Moreover, the per-residue energy contributions of the 20 hot- and warm-spot residues in two complexes of (*R*)-TSA−HDAC6 and (*S*)-TSA−HDAC6 are illustrated in Figure 7B, and the residues of significantly higher or lower contribution (≥0.5 kcal/mol) in (*R*)-TSA−HDAC6 than (*S*)-TSA−HDAC6 were marked by a light-blue five-point start or light-orange four-point star, respectively. In particular, three residues (P24, S91, and L272) in HDAC6 were marked by light-blue five-point stars, and the other three residues (F202, M205, and H174) were indicated by light-orange four-point stars. Those 3 + 3 residues of significant per-residue energy variations were then highlighted in the TSA−HDAC6-binding structures revealed by MD simulation in this work (Supplementary Figure S5). As shown, three residues in loops L1, L2, and L4 of the studied complex (*R*)-TSA−HDAC6 compensated its energy variation lost in loops L3 and L6, which then led to the relatively equivalent binding affinity of (*R*)-TSA and (*S*)-TSA in HDAC6.

Identification of the Key Residues Contributing to (*S*)-TSA's Selectivity to HDAC6. To understand the selectivity of (*S*)-TSA to HDAC6, it was of great importance to reveal the mechanism underlying its differential binding free energies between HDAC1 and HDAC6 at the per-residue energy contribution level. As shown in Figure 7C, there were six residues together with the Zn with significant energy variation favoring the binding of (*S*)-TSA to HDAC6 (each residue was marked by a light-orange four-point star), whereas only three residues with significant energy variation beneficial for the binding of (*S*)-TSA to HDAC1 (shown by the orange four-point stars) were discovered. In particular, the sum of energy differences among the residues marked by light-orange four-point stars equaled 6.8 kcal/mol, whereas that of the residues highlighted by an orange four-point star was only 2.4 kcal/mol. This result indicated that the residues marked by light-orange four-point stars played a decisive role in the selective inhibitory activity of HDAC6 by (*S*)-TSA. As shown in Figure 9, these decisive residues were basically in loops L3,

DOI: 10.1021/acschemneuro.8b00729
ACS Chem. Neurosci. 2019, 10, 2467−2480

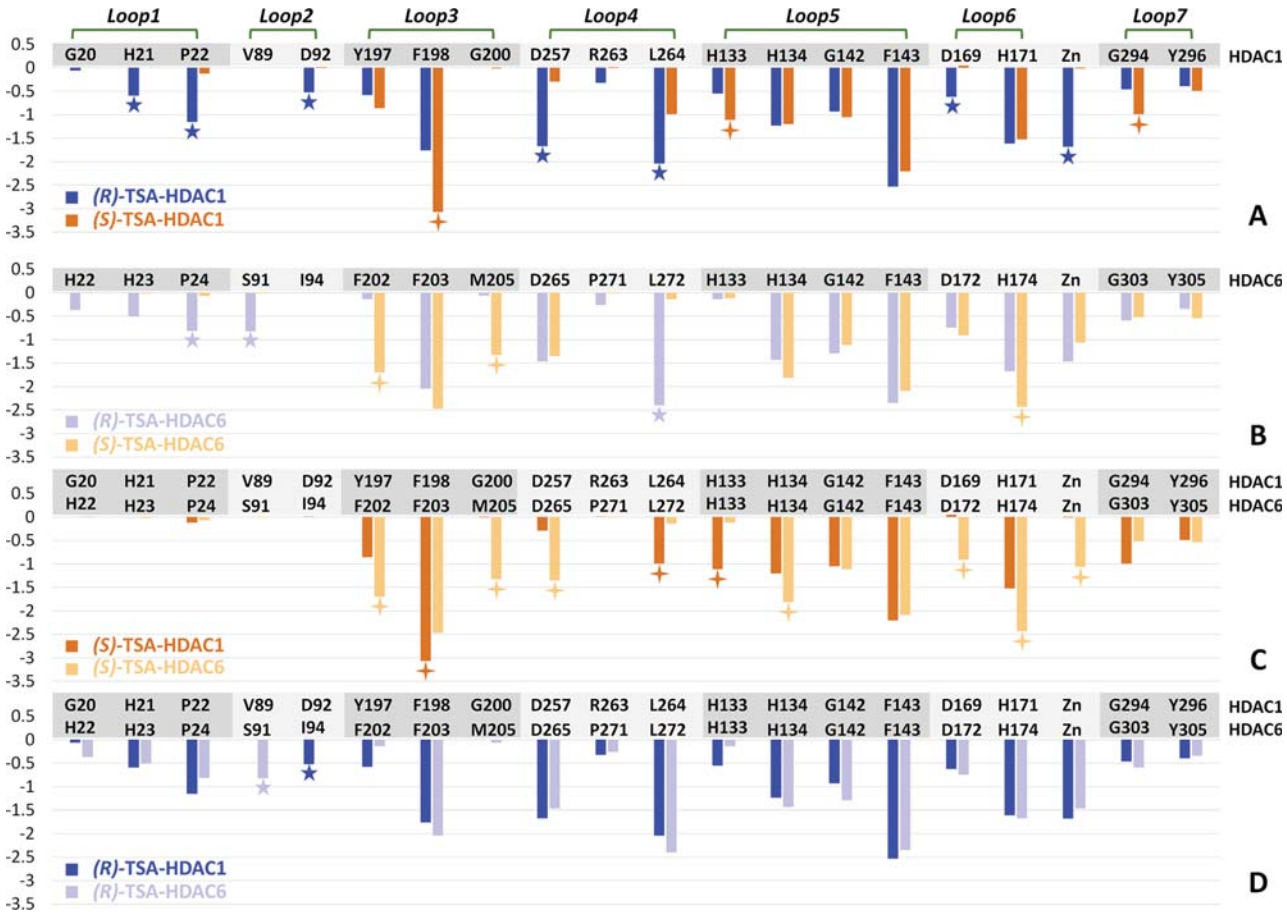

Figure 7. Per-residue binding free energy decomposition of 20 hot- and warm-spot residues in the four studied systems. All residues are ordered by their three-dimensional distribution (from loops L1 to L7), and the significant per-residue energy variation (≥0.5 kcal/mol) of a residue between any two complexes is highlighted by a star (four- or five-point star).

L4, L5, and L6. Among them, there were two nonconservative residues (G200/M205 and Y197/F202 for HDAC1/6) and four conservative residues deep inside the active pocket.

The interactions of those two nonconservative residues with (*S*)-TSA are illustrated in Figure 10. As shown, there was an obvious difference between the backbones of G200 in HDAC1 and M205 in HDAC6 (the backbone of M205 in HDAC6 was substantially larger than that of G200 in HDAC1). As illustrated in Figure 10A, this clear difference made M205 much closer to the Cap of (*S*)-TSA (3.5−4.1 Å) than G200 (8.2−8.6 Å), which substantially improved the interaction between (*S*)-TSA and M205 in HDAC6. For another nonconservative residue Y197/F202, the interactions of two residues in different subtypes with (*S*)-TSA also varied greatly. As shown in Figure 10B, the centroid of benzene in (*S*)-TSA fell vertically onto the benzene ring of HDAC6's F202, and the distance between their centers of mass was 4.9 Å. Because this distance fell in the range of a typical $\pi-\pi$ interaction, there should be a perpendicular (T-shape) $\pi-\pi$ interaction between the benzene in (*S*)-TSA and benzene ring of F202 in HDAC6.[107] However, for Y197 in HDAC1 (corresponding to F202 in HDAC6), the centroid of benzene in (*S*)-TSA did not fall onto its benzene ring, and the distance between their centers of mass (6.7 Å) was out of the range of a typical $\pi-\pi$ interaction.[107]

For the four conservative residues identified in Figure 9 (deep inside the active pocket), they interacted primarily with the zinc-binding group (ZBG) of (*S*)-TSA. Three out of the four residues surrounded Zn and collectively interacted with (*S*)-TSA, which demonstrated a key role played by these interactions in determining (*S*)-TSA's selectivity. Therefore, the distance between Zn and the carbonyl oxygen of ZBG of (*S*)-TSA was further assessed. As shown in Figure 11, the average distances of ZBG carbonyl oxygen and zinc ions were 2.2, 2.2, and 2.3 Å in (*S*)-TSA−HDAC6, (*R*)-TSA−HDAC6, and (*R*)-TSA−HDAC1, respectively, but that in (*S*)-TSA−HDAC1 was much more distant (4.2 Å) compared to the three systems above, which would substantially reduce the interaction between (*S*)-TSA and the zinc ion in HDAC1. One thing we would like to elaborate was that the average distance shown in Figure 11A−D was calculated based on the last 50 ns of the MD trajectory (substantially stable in Figure 11E).

By collectively consideration of the effects of the nonconservative residues in loop L3 and the conservative residues deep inside the active pocket, the mechanism underlying (*S*)-TSA's selectivity to HDAC6 may be revealed. As shown in Figure 9, the nonconservative residues F202 and M205 in loop L3 of HDAC6 significantly enhanced the binding of (*S*)-TSA by shortening the interacting distance and forming a $\pi-\pi$ interaction (Figure 10). Because of the rigidity of TSA, the

DOI: 10.1021/acschemneuro.8b00729
ACS Chem. Neurosci. 2019, 10, 2467−2480

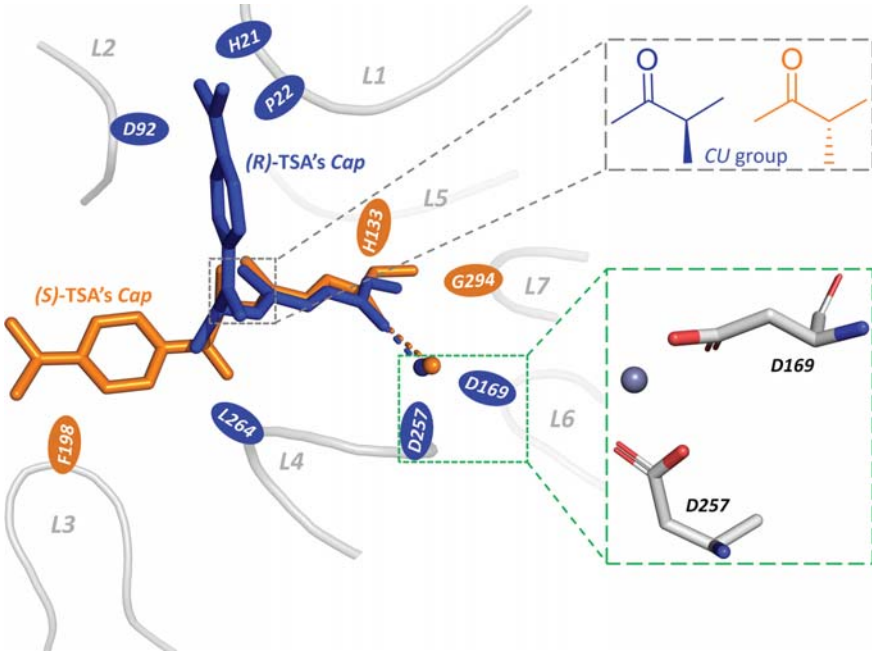

Figure 8. Nine residues of significant per-residue energy variations (identified and marked by a star in Figure 7A) are highlighted in the TSA–HDAC1-binding structures revealed by the MD simulation of this work (the blue and orange backgrounds refer to the residues beneficial for the binding of (*R*)-TSA and (*S*)-TSA in HDAC1, respectively). Cap groups of (*R*)-TSA and (*S*)-TSA orientated to different loop domains because of the chirality residing in the CU group.

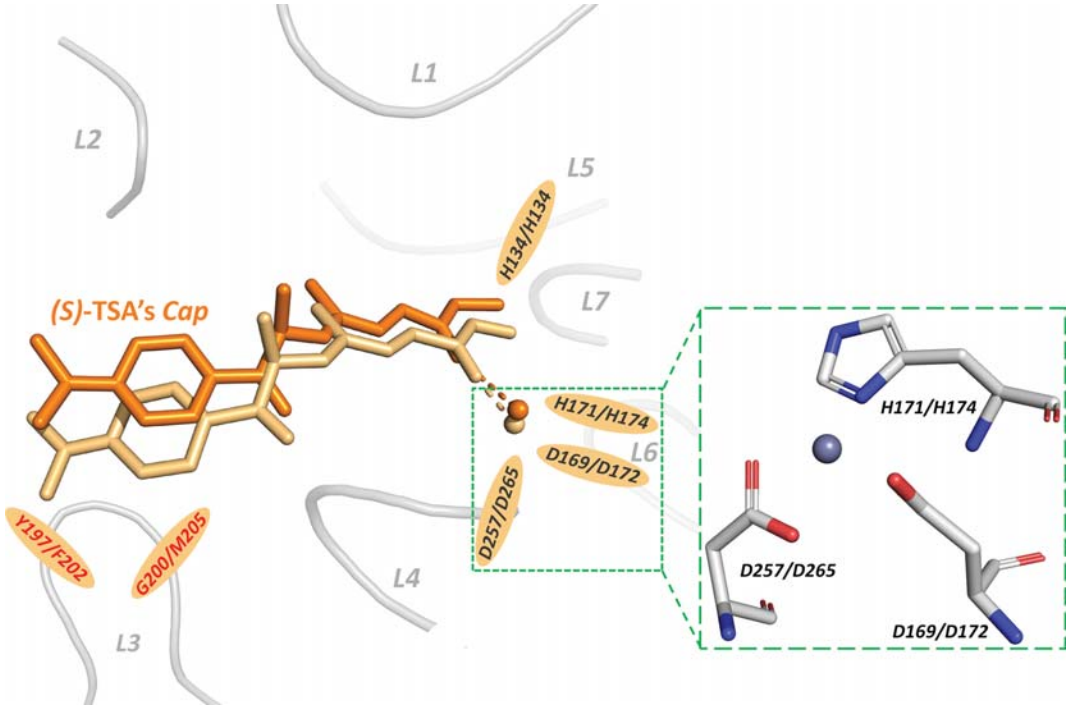

Figure 9. Six key residues decisive in (*S*)-TSA's selectivity to HDAC6 highlighted in the TSA–HDAC1-binding structures revealed by the MD simulation (the nonconservative and conservative residues are highlighted in red and black font, respectively). All conservative residues were deep inside active pocket.

enhanced interaction in the Cap of (*S*)-TSA could induce a shift in the ZBG of (*S*)-TSA, which then improved the fit of (*S*)-TSA inside active pockets. The nonconservative residues (F202 and M205) in HDAC6 might be the trigger of (*S*)-TSA's selectivity in HDAC6 and were needed to be especially considered in future drug design.

Finally, the per-residue energy contributions of hot- and warm-spot residues in the complexes of (*R*)-TSA–HDAC1

DOI: 10.1021/acschemneuro.8b00729
ACS Chem. Neurosci. 2019, 10, 2467–2480

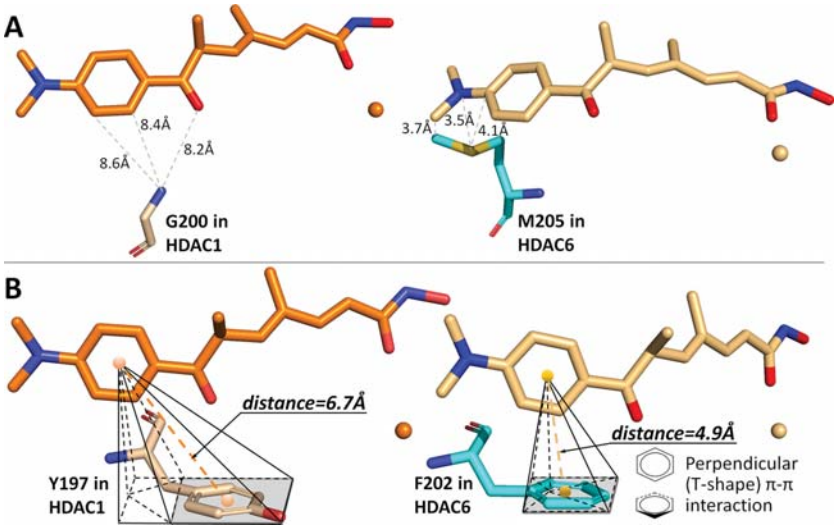

Figure 10. Interaction of (*S*)-TSA with those two nonconservative residues decisive in (*S*)-TSA's selectivity to HDAC6. (A) Difference between the backbones of G200 in HDAC1 and M205 in HDAC6 together with their modes of interaction with (*S*)-TSA; (B) the relative position between the centroid of benzene in (*S*)-TSA and the benzene ring of F202/Y197 in HDAC6/HDAC1 and the distances between their centers of mass.

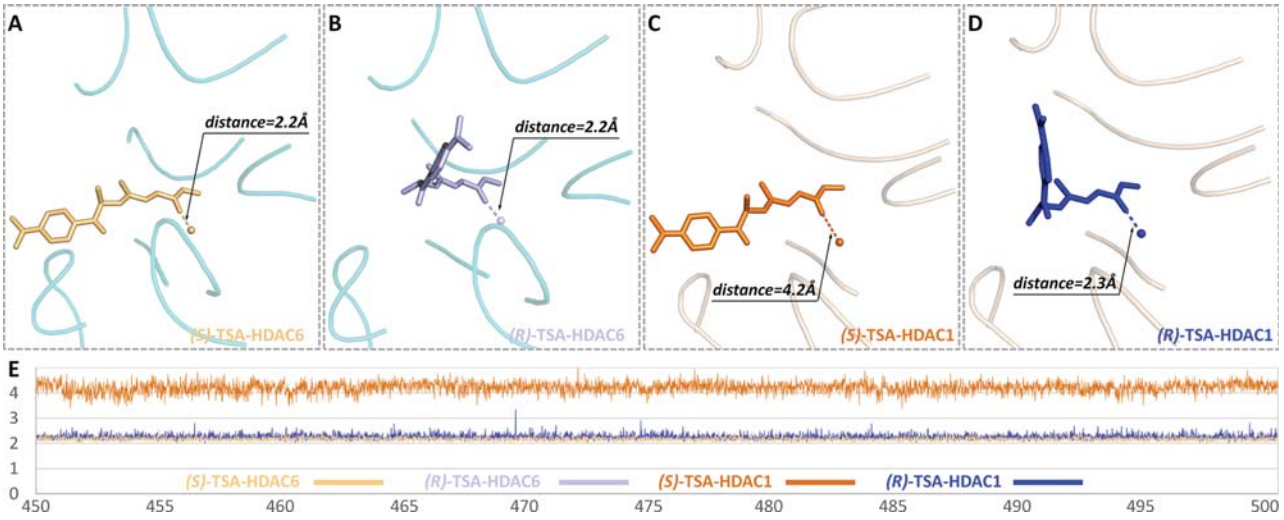

Figure 11. Average distance between the Zn and the carbonyl oxygen of ZBG of (*S*)-TSA in the complexes (A) (*S*)-TSA−HDAC6, (B) (*R*)-TSA−HDAC6, (C) (*S*)-TSA−HDAC1, and (D) (*R*)-TSA−HDAC1. The average distances were calculated based on (E) the last 50 ns of MD trajectories, which was substantially stable within this period of simulation.

and (*R*)-TSA−HDAC6 were also provided in Figure 7D, and the residues of significantly higher or lower contributions (≥0.5 kcal/mol) in (*R*)-TSA−HDAC1 and (*R*)-TSA−HDAC6 were marked by a blue or light-blue five-point star, respectively. As shown, only two residues were marked (one for the blue five-point star and another for the light-blue five-point star). These two residues were also highlighted in the TSA−HDAC1/6-binding structures revealed by MD simulation in this work (Supplementary Figure S6). Both residues were nonconservative residues, but their effects on (*R*)-TSA's binding counteracted each other, which led to the relatively equivalent binding affinity of (*R*)-TSA in HDAC1 and HDAC6.

CONCLUSION

A variety of in silico approaches were combined in this study to explore, validate, and differentiate the binding mechanisms of TSA enantiomers in HDAC1/6 at the atomic level. First, six residues (H21, P22, D92, D257, L264, and D169) in HDAC1 together with Zn were identified as playing key roles in the much higher binding affinity of (*R*)-TSA than that of (*S*)-TSA in HDAC1. Then, four conservative residues inside the active pocket and two nonconservative residues (G200/M205 and Y197/F202 in HDAC1/6) were discovered as the decisive residues of (*S*)-TSA's selectivity toward HDAC6. Finally, a mechanism underlying (*S*)-TSA's selectivity to HDAC6 was proposed, which was composed of the trigger by two nonconservative residues F202 and M205 in HDAC6 and a subsequently improved fit of (*S*)-TSA inside HDAC6's active

DOI: 10.1021/acschemneuro.8b00729
ACS Chem. Neurosci. 2019, 10, 2467−2480

pocket. Because of their decisive roles in (*S*)-TSA's selectivity to HDAC6, both F202 and M205 should be especially considered in the discovery of novel sHDAC6Is.

METHODS

Preparation of the Systems. Prior to molecular dynamic simulation, initial binding conformations of (*R*)- and (*S*)-TSA with HDAC1 and HDAC6 should be obtained through molecular docking using the *Glide* software with the default setting of standard precision.[53] The 3D structures of (*R*)-TSA and (*S*)-TSA could be obtained from *PubChem*.[54] Then, the low-energy conformations of (*R*)- and (*S*)-TSA were generated using *LigPrep*[55] (OPLS-2005 force fields[56]), and the structures of (*R*)- and (*S*)-TSA were preprocessed by *Epik*[57] (pH value = 7.0 ± 2.0). Furthermore, HDAC1 and HDAC6 structures were processed by *Maestro*[58] (adding the hydrogen atoms, minimizing the structural conformation and assigning partial charge). Until now, the crystal structures of HDAC1 and HDAC6 had been available from *Protein Data Bank*,[59] and the crystal structure of human HDAC6 complexed with (*R*)-TSA (PDB entry: 5EDU[23]) and HDAC1 with novel peptide inhibitor (PDB entry: 5ICN[60]) could give researchers valuable instructions on determining the binding site and defining the docking grid box. Thus, (*R*)-TSA in 5EDU and the novel peptide inhibitor in 5ICN were adopted as the references when defining the docking grid box by the Receptor Grid Generation tool embedded in *Glide*; detailed information is available in the Supplementary Method. Finally, to ensure the effectiveness of molecular docking, X-ray structures of *Danio rerio* HDAC6 with various ligands (PDB ID: 5WGM,[21] 5G0H,[50] and 5G0J[50]) were used to conduct cross-docking using *Glide*[53] by the following two steps. First, the ligands and proteins were prepared in the same way as described above, and the docking grid boxes were determined by centering the initial ligands in the X-ray structures chosen for cross-docking using the Receptor Grid Generation tool in *Glide*.[53] Then, the prepared (*R*)- and (*S*)-TSA were cross-docked into the selected PDB structures (5WGM, 5G0H, and 5G0J) with the same parameters as those of the system preparation.

In previous studies, the zinc ion is largely deprived in searching conformational complexity and binding property of the inhibitors complexed with HDAC6[61] and screening/designing novel HDAC inhibitors.[62] However, zinc was reported to play an essential role in catalyzing the hydrolysis of acetyl−lysine amide bonds,[63] and HDAC inhibitors exert their inhibitory activity mainly by competing with HDAC catalytic centers for the zinc ion.[64] Moreover, previous analysis revealed that the binding complex would be unstable and break up within nanoseconds during simulation without the proper process of the zinc ion,[65] and the coordinates of zinc without the process of appropriate field parameters were found to fluctuate greatly during molecular simulation.[66] Therefore, zinc was considered in many current protein systems for stabilizing the oligomer or maintaining the binding site.[67,68] In this study, in order to extensively consider zinc in HDAC complexes, a recently proposed nonbonded model 126-4[69] was applied and validated in this study. During the MD simulation, the binding site fluctuated slightly, and the decomposition free energy of zinc was calculated to assess its interaction with ZBG.

Molecular Dynamics (MD) Simulation. MD simulation was conducted using GPU-accelerated PMEMD in *AMBER16*[70] on 16 cores of an array of two 2.6 GHz Intel Xeon E5-2650v2 processors and four pieces of NVIDIA Tesla K40C graphic cards. First, the enzymes and their corresponding TSA enantiomers were processed using the AMBER *ff14SB*[71] and general *Amber* force fields,[72] and the Li/Merz ion parameters for the SPC/E water models were directly adopted from previous publications.[73−75] Then, the restrained electrostatic potential atomic partial charge was assigned to (*R*)- and (*S*)-TSA by *antechamber*,[76] and *Gaussian 09* was adopted to process the geometry optimization and calculate the electrostatic potential (Supplementary Method). Prior to MD simulation, the initial energy of the prepared system was minimized using two sequential procedures: (1) conducting harmonic restraints on all solute atoms[77] and (2) releasing atoms to move freely. Within each procedure, the first 5000 steps were conducted using the steepest descent method, and the subsequent 5000 steps were accomplished using the conjugated gradient method.[78−80] Third, each studied complex was heated by two steps: (1) from 0 gradually to 100 K and (2) subsequently to 310 K[81] (Supplementary Method). Fourth, a 5 ns unrestrained simulation at 310 K was added for equilibrating periodic boundary conditions for all studied systems.[82,83] At last, a 500 ns unrestrained MD simulation was systematically conducted for the prepared four complexes under the temperature of 310 K and the pressure of 1 atm.[84,85] Temperature was controlled by Langevin dynamics, and pressure was controlled using *Monte Carlo barostat*.[86−88] In all simulations, the long-range electrostatic interaction was processed,[89] and all interacting bonds were kept rigid.[90−92] All analyses of MD trajectories (RMSD, representative structure and binding free energy) were conducted by *cpptraj* and *mm_pbsa.pl* programs in *AMBER16*,[70] and *PyMOL* was used to visualize the structures of studied systems.[93] Detailed information is provided in the Supplementary Method.

Thermodynamic Calculation and Hot- and Warm-Spot Identification by Hierarchical Clustering. The binding free energy (BFE) of (*R*)- and (*S*)-TSA to HDAC1 and HDAC6 neglecting the entropic contribution was assessed by the MM-GBSA approach provided in *AMBER16*,[94] and a total of 1000 snapshots were retrieved from an equilibrated trajectory between 400 and 500 ns to calculate the BFE and the per-residue decomposed energy. Detailed descriptions of the equations for calculating these energies are provided and discussed in the Supplementary Method. The residues with energy contributions in HDACs to TSA's binding were selected to generate vectors of four dimensions. The clustering tree of these residues with energy contribution to (*R*) and (*S*)-TSA's binding (>0.1 kcal/mol) in HDACs was constructed by the *R* analysis package.[95] Then, the online tree generator *iTOL* was used to draw the hierarchical tree graphs.[96] Detailed description is provided and discussed in the Supplementary Method.

ASSOCIATED CONTENT

Supporting Information

The Supporting Information is available free of charge on the ACS Publications website at DOI: 10.1021/acschemneuro.8b00729.

Figure S1: The chemical structures of the representative selective inhibitor of HDAC6 (sHDAC6I); Figure S2: Structural superimposition between (A) the cross-docking poses of (*R*)-TSA (wheat) and the structure of (*R*)-TSA (cyan) bound to HDAC8 as well as (B) the cross-docking poses of (*S*)-TSA (magenta) and the structure of (*S*)-TSA (yellow) bound to Danio rerio HDAC6; Figure S3: The structural alignment of the docked poses (yellow) and their corresponding representative snapshots (green) of MD simulation for the four studied systems. (A) (*R*)-TSA in HDAC1, (B) (*R*)-TSA in HDAC6, (C) (*S*)-TSA in HDAC1, and (D) (*R*)-TSA in HDAC6; Figure S4: Structural superimpositions between representative snapshots and cocrystallized structures. The structural alignments of (A) (*R*)-TSA−HDAC6 (magenta) and 5WGI1 (white), (B) (*S*)-TSA−HDAC6 (slate) and 5G0H33 (green), (C) (*R*)/(*S*)-TSA−HDAC1 (cyan/salmon) and 4QA334 (yellow); Figure S5: Six residues of significant per-residue energy contribution to the binding of (*R*)-TSA or (*S*)-TSA in HDAC6 highlighted in the TSA−HDAC6-binding structures revealed by the MD simulation of this work (the light-blue and light-orange backgrounds refer to the residues beneficial for (*R*)-

DOI: 10.1021/acschemneuro.8b00729
ACS Chem. Neurosci. 2019, 10, 2467−2480

TSA's and (*S*)-TSA's binding in HDAC1, respectively); Figure S6: Two residues of significant per-residue energy contribution to (*R*)-TSA's binding in HDAC1 or HDAC6 highlighted in the TSA−HDAC6-binding structures revealed by MD simulation of this work (blue and light-blue backgrounds refer to the residues beneficial for (*R*)-TSA's binding in HDAC6 and HDAC1, respectively) (PDF)

AUTHOR INFORMATION

Corresponding Authors

*E-mail: zhufeng@zju.edu.cn; Phone: +86-(0)571-8820-8444 (F.Z.)

*E-mail: xueww@cqu.edu.cn; Phone: +86-(0)23-6567-8468 (W.X.)

ORCID

Yunqing Qiu: 0000-0003-0899-2019

Wei Wei Xue: 0000-0002-3285-0574

Feng Zhu: 0000-0001-8069-0053

Author Contributions

F.Z. and W.X. conceived the work and directed the experiments; Y.Z. performed the MD simulations; Y.Z., J.Y., T.F., and G.Z. collected and confirmed the data of protein and ligand structures; Y.Z., J.H., F.L., Y.L., Y.Q., and F.Y. performed the analysis. F.Z. and Y.Z. drafted the first and second versions of the manuscript. All authors read, edited, and approved the final version of manuscript.

Funding

National Natural Science Foundation of China (81872798), National Key Research and Development Program of China (2018YFC0910500), Innovation Project on Industrial Generic Key Technologies of Chongqing (cstc2015zdcy-ztzx120003), and Fundamental Research Funds for the Central Universities (2018QNA7023, 10611CDJXZ238826, 2018CDQYSG0007, CDJZR14468801, CDJKXB14011).

Notes

The authors declare no competing financial interest.

ABBREVIATIONS

Cap, capping group; CD, catalytic domain; CU, connect unit; HATs, histone acetyltransferases; HDAC6, histone deacetylase 6; HDACi, HDAC inhibitors; MD, molecular dynamics; MM/GBSA, molecular mechanics generalized Born surface area; sHDAC6Is, selectivity of HDAC6 inhibitors; TSA, Trichostatin A; ZBG, zinc-binding group

REFERENCES

(1) Butler, R., and Bates, G. P. (2006) Histone deacetylase inhibitors as therapeutics for polyglutamine disorders. *Nat. Rev. Neurosci. 7*, 784−796.

(2) Okugawa, Y., Grady, W. M., and Goel, A. (2015) Epigenetic alterations in colorectal cancer: emerging biomarkers. *Gastroenterology 149*, 1204−1225.

(3) Lao, V. V., and Grady, W. M. (2011) Epigenetics and colorectal cancer. *Nat. Rev. Gastroenterol. Hepatol. 8*, 686−700.

(4) DaRosa, P. A., Harrison, J. S., Zelter, A., Davis, T. N., Brzovic, P., Kuhlman, B., and Klevit, R. E. (2018) A bifunctional role for the UHRF1 UBL domain in the control of hemi-methylated DNA-dependent histone ubiquitylation. *Mol. Cell 72*, 753−765.

(5) Zeng, X., Liu, L., Lu, L., and Zou, Q. (2018) Prediction of potential disease-associated microRNAs using structural perturbation method. *Bioinformatics 34*, 2425−2432.

(6) Zou, Q., Xing, P., Wei, L., and Liu, B. (2019) Gene2vec: gene subsequence embedding for prediction of mammalian N (6)-methyladenosine sites from mRNA. *RNA 25*, 205−218.

(7) He, W., Ju, Y., Zeng, X., Liu, X., and Zou, Q. (2018) ScncDNAPred: a sequence-based predictor for identifying non-coding DNA in saccharomyces cerevisiae. *Front. Microbiol. 9*, 2174.

(8) Minucci, S., and Pelicci, P. G. (2006) Histone deacetylase inhibitors and the promise of epigenetic (and more) treatments for cancer. *Nat. Rev. Cancer 6*, 38−51.

(9) Haberland, M., Montgomery, R. L., and Olson, E. N. (2009) The many roles of histone deacetylases in development and physiology: implications for disease and therapy. *Nat. Rev. Genet. 10*, 32−42.

(10) de Ruijter, A. J. M., van Gennip, A. H., Caron, H. N., Kemp, S., and van Kuilenburg, A. B. P. (2003) Histone deacetylases (HDACs): characterization of the classical HDAC family. *Biochem. J. 370*, 737−749.

(11) Zhu, F., Li, X. X., Yang, S. Y., and Chen, Y. Z. (2018) Clinical success of drug targets prospectively predicted by in silico study. *Trends Pharmacol. Sci. 39*, 229−231.

(12) Parbin, S., Kar, S., Shilpi, A., Sengupta, D., Deb, M., Rath, S. K., and Patra, S. K. (2014) Histone deacetylases: a saga of perturbed acetylation homeostasis in cancer. *J. Histochem. Cytochem. 62*, 11−33.

(13) Falkenberg, K. J., and Johnstone, R. W. (2014) Histone deacetylases and their inhibitors in cancer, neurological diseases and immune disorders. *Nat. Rev. Drug Discovery 13*, 673−691.

(14) He, W., Wei, L., and Zou, Q. (2018) Research progress in protein posttranslational modification site prediction. *Briefings Funct. Genomics*, 1−10.

(15) Johnstone, R. W. (2002) Histone-deacetylase inhibitors: novel drugs for the treatment of cancer. *Nat. Rev. Drug Discovery 1*, 287−299.

(16) Gradilone, S. A., Radtke, B. N., Bogert, P. S., Huang, B. Q., Gajdos, G. B., and LaRusso, N. F. (2013) HDAC6 inhibition restores ciliary expression and decreases tumor growth. *Cancer Res. 73*, 2259−2270.

(17) Kaliszczak, M., van Hechanova, E., Li, Y., Alsadah, H., Parzych, K., Auner, H. W., and Aboagye, E. O. (2018) The HDAC6 inhibitor C1A modulates autophagy substrates in diverse cancer cells and induces cell death. *Br. J. Cancer 119*, 1278−1287.

(18) Li, T., Zhang, C., Hassan, S., Liu, X., Song, F., Chen, K., Zhang, W., and Yang, J. (2018) Histone deacetylase 6 in cancer. *J. Hematol. Oncol. 11*, 111.

(19) Brindisi, M., Senger, J., Cavella, C., Grillo, A., Chemi, G., Gemma, S., Cucinella, D. M., Lamponi, S., Sarno, F., Iside, C., Nebbioso, A., Novellino, E., Shaik, T. B., Romier, C., Herp, D., Jung, M., Butini, S., Campiani, G., Altucci, L., and Brogi, S. (2018) Novel spiroindoline HDAC inhibitors: synthesis, molecular modelling and biological studies. *Eur. J. Med. Chem. 157*, 127−138.

(20) Yu, C. W., Hung, P. Y., Yang, H. T., Ho, Y. H., Lai, H. Y., Cheng, Y. S., and Chern, J. W. (2019) Quinazolin-2,4-dione-based hydroxamic acids as selective histone deacetylase-6 inhibitors for treatment of non-small-cell lung cancer. *J. Med. Chem. 62*, 857.

(21) Porter, N. J., Mahendran, A., Breslow, R., and Christianson, D. W. (2017) Unusual zinc-binding mode of HDAC6-selective hydroxamate inhibitors. *Proc. Natl. Acad. Sci. U. S. A. 114*, 13459−13464.

(22) Wei, L. Y., Ding, Y. J., Su, R., Tang, J. J., and Zou, Q. (2018) Prediction of human protein subcellular localization using deep learning. *J. Parallel Distr. Com. 117*, 212−217.

(23) Hai, Y., and Christianson, D. W. (2016) Histone deacetylase 6 structure and molecular basis of catalysis and inhibition. *Nat. Chem. Biol. 12*, 741−747.

(24) Haggarty, S. J., Koeller, K. M., Wong, J. C., Grozinger, C. M., and Schreiber, S. L. (2003) Domain-selective small-molecule inhibitor of histone deacetylase 6 (HDAC6)-mediated tubulin deacetylation. *Proc. Natl. Acad. Sci. U. S. A. 100*, 4389−4394.

DOI: 10.1021/acschemneuro.8b00729
ACS Chem. Neurosci. 2019, 10, 2467−2480

(25) Lee, J. B., Wei, J., Liu, W., Cheng, J., Feng, J., and Yan, Z. (2012) Histone deacetylase 6 gates the synaptic action of acute stress in prefrontal cortex. *J. Physiol. 590*, 1535−1546.
(26) Fukada, M., Hanai, A., Nakayama, A., Suzuki, T., Miyata, N., Rodriguiz, R. M., Wetsel, W. C., Yao, T. P., and Kawaguchi, Y. (2012) Loss of deacetylation activity of Hdac6 affects emotional behavior in mice. *PLoS One 7*, No. e30924.
(27) Espallergues, J., Teegarden, S. L., Veerakumar, A., Boulden, J., Challis, C., Jochems, J., Chan, M., Petersen, T., Deneris, E., Matthias, P., Hahn, C. G., Lucki, I., Beck, S. G., and Berton, O. (2012) HDAC6 regulates glucocorticoid receptor signaling in serotonin pathways with critical impact on stress resilience. *J. Neurosci. 32*, 4400−4416.
(28) Kim, J. W., Kwon, O. Y., and Kim, M. H. (2007) Differentially expressed genes and morphological changes during lengthened immobilization in rat soleus muscle. *Differentiation 75*, 147−157.
(29) Vanaja, G. R., Ramulu, H. G., and Kalle, A. M. (2018) Overexpressed HDAC8 in cervical cancer cells shows functional redundancy of tubulin deacetylation with HDAC6. *Cell Commun. Signaling 16*, 20.
(30) Zhang, L., Sheng, S., and Qin, C. (2012) The role of HDAC6 in Alzheimer's disease. *J. Alzheimer's Dis. 33*, 283−295.
(31) Guo, W., Naujock, M., Fumagalli, L., Vandoorne, T., Baatsen, P., Boon, R., Ordovas, L., Patel, A., Welters, M., Vanwelden, T., et al. (2017) HDAC6 inhibition reverses axonal transport defects in motor neurons derived from FUS-ALS patients. *Nat. Commun. 8*, 861.
(32) Bruserud, O., Stapnes, C., Ersvaer, E., Gjertsen, B. T., and Ryningen, A. (2007) Histone deacetylase inhibitors in cancer treatment: a review of the clinical toxicity and the modulation of gene expression in cancer cell. *Curr. Pharm. Biotechnol. 8*, 388−400.
(33) Choi, E. W., Song, J. W., Ha, N., Choi, Y. I., and Kim, S. (2018) CKD-506, a novel HDAC6-selective inhibitor, improves renal outcomes and survival in a mouse model of systemic lupus erythematosus. *Sci. Rep. 8*, 17297.
(34) Thomas, E. A. (2009) Focal nature of neurological disorders necessitates isotype-selective histone deacetylase (HDAC) inhibitors. *Mol. Neurobiol. 40*, 33−45.
(35) Wang, L., Chan, C. E. L., Wong, A. L., Wong, F. C., Lim, S. W., Chinnathambi, A., Alharbi, S. A., Lee, L. S., Soo, R., Yong, W. P., et al. (2017) Combined use of irinotecan with histone deacetylase inhibitor belinostat could cause severe toxicity by inhibiting SN-38 glucuronidation via UGT1A1. *Oncotarget 8*, 41572−41581.
(36) Gupta, P., Reid, R. C., Iyer, A., Sweet, M. J., and Fairlie, D. P. (2012) Towards isozyme-selective HDAC inhibitors for interrogating disease. *Curr. Top. Med. Chem. 12*, 1479−1499.
(37) Butler, K. V., Kalin, J., Brochier, C., Vistoli, G., Langley, B., and Kozikowski, A. P. (2010) Rational design and simple chemistry yield a superior, neuroprotective HDAC6 inhibitor, tubastatin A. *J. Am. Chem. Soc. 132*, 10842−10846.
(38) Bergman, J. A., Woan, K., Perez-Villarroel, P., Villagra, A., Sotomayor, E. M., and Kozikowski, A. P. (2012) Selective histone deacetylase 6 inhibitors bearing substituted urea linkers inhibit melanoma cell growth. *J. Med. Chem. 55*, 9891−9899.
(39) Amengual, J. E., Johannet, P., Lombardo, M., Zullo, K., Hoehn, D., Bhagat, G., Scotto, L., Jirau-Serrano, X., Radeski, D., Heinen, J., Jiang, H., Cremers, S., Zhang, Y., Jones, S., and O'Connor, O. A. (2015) Dual targeting of protein degradation pathways with the selective HDAC6 inhibitor ACY-1215 and bortezomib is synergistic in lymphoma. *Clin. Cancer Res. 21*, 4663−4675.
(40) Lee, J. H., Mahendran, A., Yao, Y., Ngo, L., Venta-Perez, G., Choy, M. L., Kim, N., Ham, W. S., Breslow, R., and Marks, P. A. (2013) Development of a histone deacetylase 6 inhibitor and its biological effects. *Proc. Natl. Acad. Sci. U. S. A. 110*, 15704−15709.
(41) Giannini, G., Vesci, L., Battistuzzi, G., Vignola, D., Milazzo, F. M., Guglielmi, M. B., Barbarino, M., Santaniello, M., Fanto, N., Mor, M., Rivara, S., Pala, D., Taddei, M., Pisano, C., and Cabri, W. (2014) ST7612AA1, a thioacetate-omega(gamma-lactam carboxamide) derivative selected from a novel generation of oral HDAC inhibitors. *J. Med. Chem. 57*, 8358−8377.
(42) Blackburn, C., Barrett, C., Chin, J., Garcia, K., Gigstad, K., Gould, A., Gutierrez, J., Harrison, S., Hoar, K., Lynch, C., Rowland, R. S., Tsu, C., Ringeling, J., and Xu, H. (2013) Potent histone deacetylase inhibitors derived from 4-(aminomethyl)-N-hydroxybenzamide with high selectivity for the HDAC6 isoform. *J. Med. Chem. 56*, 7201−7211.
(43) Wang, X. X., Wan, R. Z., and Liu, Z. P. (2018) Recent advances in the discovery of potent and selective HDAC6 inhibitors. *Eur. J. Med. Chem. 143*, 1406−1418.
(44) Mackwitz, M. K. W., Hamacher, A., Osko, J. D., Held, J., Scholer, A., Christianson, D. W., Kassack, M. U., and Hansen, F. K. (2018) Multicomponent synthesis and binding mode of imidazo[1,2-a]pyridine-capped selective HDAC6 inhibitors. *Org. Lett. 20*, 3255−3258.
(45) Wagner, F. F., Olson, D. E., Gale, J. P., Kaya, T., Weiwer, M., Aidoud, N., Thomas, M., Davoine, E. L., Lemercier, B. C., Zhang, Y. L., and Holson, E. B. (2013) Potent and selective inhibition of histone deacetylase 6 (HDAC6) does not require a surface-binding motif. *J. Med. Chem. 56*, 1772−1776.
(46) Kalin, J. H., and Bergman, J. A. (2013) Development and therapeutic implications of selective histone deacetylase 6 inhibitors. *J. Med. Chem. 56*, 6297−6313.
(47) Zou, Q., Qu, K., Luo, Y., Yin, D., Ju, Y., and Tang, H. (2018) Predicting diabetes mellitus with machine learning techniques. *Front. Genet. 9*, 515.
(48) Li, B., Tang, J., Yang, Q., Li, S., Cui, X., Li, Y., Chen, Y., Xue, W., Li, X., and Zhu, F. (2017) NOREVA: normalization and evaluation of MS-based metabolomics data. *Nucleic Acids Res. 45*, W162−W170.
(49) Li, B., Tang, J., Yang, Q., Cui, X., Li, S., Chen, S., Cao, Q., Xue, W., Chen, N., and Zhu, F. (2016) Performance evaluation and online realization of data-driven normalization methods used in LC/MS based untargeted metabolomics analysis. *Sci. Rep. 6*, 38881.
(50) Miyake, Y., Keusch, J. J., Wang, L., Saito, M., Hess, D., Wang, X., Melancon, B. J., Helquist, P., Gut, H., and Matthias, P. (2016) Structural insights into HDAC6 tubulin deacetylation and its selective inhibition. *Nat. Chem. Biol. 12*, 748−754.
(51) Hanson, K., Tian, N., Vickers, J. C., and King, A. E. (2018) The HDAC6 inhibitor Trichostatin A acetylates microtubules and protects axons from excitotoxin-induced degeneration in a compartmented culture model. *Front. Neurosci. 12*, 872.
(52) Yoshida, M., Hoshikawa, Y., Koseki, K., Mori, K., and Beppu, T. (1990) Structural specificity for biological-activity of Trichostatin-a, a specific inhibitor of mammalian-cell cycle with potent differentiation-inducing activity in friend-leukemia cells. *J. Antibiot. 43*, 1101−1106.
(53) (2009) *Glide, version 5.5*, Schrödinger, LLC, New York.
(54) Kim, S., Thiessen, P. A., Bolton, E. E., Chen, J., Fu, G., Gindulyte, A., Han, L., He, J., He, S., Shoemaker, B. A., et al. (2016) PubChem substance and compound databases. *Nucleic Acids Res. 44*, D1202−D1213.
(55) (2009) *LigPrep, version 2.3*, Schrödinger, LLC, New York.
(56) Kaminski, G. A., Friesner, R. A., Tirado-Rives, J., and Jorgensen, W. L. (2001) Evaluation and reparametrization of the OPLS-AA force field for proteins via comparison with accurate quantum chemical calculations on peptides. *J. Phys. Chem. B 105*, 6474−6487.
(57) (2009) *Epik, version 2.0*, Schrödinger, LLC, New York.
(58) (2009) *Maestro, version 9.0*, Schrödinger, LLC, New York.
(59) Berman, H. M., Westbrook, J., Feng, Z., Gilliland, G., Bhat, T. N., Weissig, H., Shindyalov, I. N., and Bourne, P. E. (2000) The protein data bank. *Nucleic Acids Res. 28*, 235−242.
(60) Watson, P. J., Millard, C. J., Riley, A. M., Robertson, N. S., Wright, L. C., Godage, H. Y., Cowley, S. M., Jamieson, A. G., Potter, B. V., and Schwabe, J. W. (2016) Insights into the activation mechanism of class I HDAC complexes by inositol phosphates. *Nat. Commun. 7*, 11262.
(61) Sixto-Lopez, Y., Bello, M., Rodriguez-Fonseca, R. A., Rosales-Hernandez, M. C., Martinez-Archundia, M., Gomez-Vidal, J. A., and

DOI: 10.1021/acschemneuro.8b00729
ACS Chem. Neurosci. 2019, 10, 2467−2480

Correa-Basurto, J. (2017) Searching the conformational complexity and binding properties of HDAC6 through docking and molecular dynamic simulations. *J. Biomol. Struct. Dyn. 35*, 2794−2814.
(62) Zhou, H., Wang, C., Deng, T., Tao, R., and Li, W. (2018) Novel urushiol derivatives as HDAC8 inhibitors: rational design, virtual screening, molecular docking and molecular dynamics studies. *J. Biomol. Struct. Dyn. 36*, 1966−1978.
(63) Lahm, A., Paolini, C., Pallaoro, M., Nardi, M. C., Jones, P., Neddermann, P., Sambucini, S., Bottomley, M. J., Lo Surdo, P., Carfi, A., Koch, U., De Francesco, R., Steinkuhler, C., and Gallinari, P. (2007) Unraveling the hidden catalytic activity of vertebrate class IIa histone deacetylases. *Proc. Natl. Acad. Sci. U. S. A. 104*, 17335−17340.
(64) Miller, T. A., Witter, D. J., and Belvedere, S. (2003) Histone deacetylase inhibitors. *J. Med. Chem. 46*, 5097−5116.
(65) Sixto-Lopez, Y., Bello, M., and Correa-Basurto, J. (2018) Insights into structural features of HDAC1 and its selectivity inhibition elucidated by Molecular dynamic simulation and Molecular Docking. *J. Biomol. Struct. Dyn. 1*, 1−27.
(66) Hassanzadeh, M., Bagherzadeh, K., and Amanlou, M. (2016) A comparative study based on docking and molecular dynamics simulations over HDAC-tubulin dual inhibitors. *J. Mol. Graphics Modell. 70*, 170−180.
(67) Xu, L., Shan, S., Chen, Y., Wang, X., Nussinov, R., and Ma, B. (2015) Coupling of zinc-binding and secondary structure in nonfibrillar Abeta40 peptide oligomerization. *J. Chem. Inf. Model. 55*, 1218−1230.
(68) Chen, J., Wang, J., and Zhu, W. (2017) Zinc ion-induced conformational changes in new Delphi metallo-beta-lactamase 1 probed by molecular dynamics simulations and umbrella sampling. *Phys. Chem. Chem. Phys. 19*, 3067−3075.
(69) Li, P., Song, L. F., and Merz, K. M. (2015) Parameterization of highly charged metal ions using the 12−6-4 LJ-type nonbonded model in explicit water. *J. Phys. Chem. B 119*, 883−895.
(70) (2016) *AMBER, version 16*, University of California, San Francisco.
(71) Hornak, V., Abel, R., Okur, A., Strockbine, B., Roitberg, A., and Simmerling, C. (2006) Comparison of multiple Amber force fields and development of improved protein backbone parameters. *Proteins: Struct., Funct., Genet. 65*, 712−725.
(72) Wang, J., Wolf, R. M., Caldwell, J. W., Kollman, P. A., and Case, D. A. (2004) Development and testing of a general amber force field. *J. Comput. Chem. 25*, 1157−1174.
(73) Li, P., and Merz, K. M. (2014) Taking into account the ion-induced dipole interaction in the nonbonded model of ions. *J. Chem. Theory Comput. 10*, 289−297.
(74) Li, P., Song, L. F., and Merz, K. M. (2015) Systematic parameterization of monovalent ions employing the nonbonded model. *J. Chem. Theory Comput. 11*, 1645−1657.
(75) Li, P., Roberts, B. P., Chakravorty, D. K., and Merz, K. M. (2013) Rational design of particle mesh ewald compatible lennard-jones parameters for + 2 metal cations in explicit solvent. *J. Chem. Theory Comput. 9*, 2733−2748.
(76) Wang, J., Wang, W., Kollman, P. A., and Case, D. A. (2006) Automatic atom type and bond type perception in molecular mechanical calculations. *J. Mol. Graphics Modell. 25*, 247−260.
(77) Xue, W., Yang, F., Wang, P., Zheng, G., Chen, Y., Yao, X., and Zhu, F. (2018) What contributes to serotonin-norepinephrine reuptake inhibitors' dual-targeting mechanism? The key role of transmembrane domain 6 in human serotonin and norepinephrine transporters revealed by molecular dynamics simulation. *ACS Chem. Neurosci. 9*, 1128−1140.
(78) Zheng, G., Xue, W., Wang, P., Yang, F., Li, B., Li, X., Li, Y., Yao, X., and Zhu, F. (2016) Exploring the inhibitory mechanism of approved selective norepinephrine reuptake inhibitors and reboxetine enantiomers by molecular dynamics study. *Sci. Rep. 6*, 26883.
(79) Tu, G., Fu, T., Yang, F., Yao, L., Xue, W., and Zhu, F. (2018) Prediction of GluN2B-CT1290−1310/DAPK1 interaction by protein-peptide docking and molecular dynamics simulation. *Molecules 23*, 3018.
(80) Wang, Q., Xu, J., Li, Y., Huang, J., Jiang, Z., Wang, Y., Liu, L., Leung, E. L. H., and Yao, X. (2018) Identification of a novel protein arginine methyltransferase 5 inhibitor in non-small cell lung cancer by structure-based virtual screening. *Front. Pharmacol. 9*, 173.
(81) Fu, T., Zheng, G., Tu, G., Yang, F., Chen, Y., Yao, X., Li, X., Xue, W., and Zhu, F. (2018) Exploring the binding mechanism of metabotropic glutamate receptor 5 negative allosteric modulators in clinical trials by molecular dynamics simulations. *ACS Chem. Neurosci. 9*, 1492−1502.
(82) Wang, P., Fu, T., Zhang, X., Yang, F., Zheng, G., Xue, W., Chen, Y., Yao, X., and Zhu, F. (2017) Differentiating physicochemical properties between NDRIs and sNRIs clinically important for the treatment of ADHD. *Biochim. Biophys. Acta, Gen. Subj. 1861*, 2766−2777.
(83) Xue, W., Wang, P., Tu, G., Yang, F., Zheng, G., Li, X., Li, X., Chen, Y., Yao, X., and Zhu, F. (2018) Computational identification of the binding mechanism of a triple reuptake inhibitor amitifadine for the treatment of major depressive disorder. *Phys. Chem. Chem. Phys. 20*, 6606−6616.
(84) Zheng, G., Yang, F., Fu, T., Tu, G., Chen, Y., Yao, X., Xue, W., and Zhu, F. (2018) Computational characterization of the selective inhibition of human norepinephrine and serotonin transporters by an escitalopram scaffold. *Phys. Chem. Chem. Phys. 20*, 29513−29527.
(85) Yang, F. Y., Fu, T. T., Zhang, X. Y., Hu, J., Xue, W. W., Zheng, G. X., Li, B., Li, Y. H., Yao, X. J., and Zhu, F. (2017) Comparison of computational model and X-ray crystal structure of human serotonin transporter: potential application for the pharmacology of human monoamine transporters. *Mol. Simul. 43*, 1089−1098.
(86) Yang, F., Zheng, G., Fu, T., Li, X., Tu, G., Li, Y. H., Yao, X., Xue, W., and Zhu, F. (2018) Prediction of the binding mode and resistance profile for a dual-target pyrrolyl diketo acid scaffold against HIV-1 integrase and reverse-transcriptase-associated ribonuclease H. *Phys. Chem. Chem. Phys. 20*, 23873−23884.
(87) Zheng, G., Xue, W., Yang, F., Zhang, Y., Chen, Y., Yao, X., and Zhu, F. (2017) Revealing vilazodone's binding mechanism underlying its partial agonism to the 5-HT1A receptor in the treatment of major depressive disorder. *Phys. Chem. Chem. Phys. 19*, 28885−28896.
(88) Xue, W., Fu, T., Zheng, G., Tu, G., Zhang, Y., Yang, F., Tao, L., Yao, L., and Zhu, F. (2018) Recent advances and challenges of the drugs acting on monoamine transporters. *Curr. Med. Chem.* E-pub Ahead of Print..
(89) Darden, T., York, D., and Pedersen, L. (1993) Particle mesh Ewald: an N·log(N) method for Ewald sums in large systems. *J. Chem. Phys. 98*, 10089−10092.
(90) Larini, L., Mannella, R., and Leporini, D. (2007) Langevin stabilization of molecular-dynamics simulations of polymers by means of quasisymplectic algorithms. *J. Chem. Phys. 126*, 104101.
(91) Wang, P., Zhang, X., Fu, T., Li, S., Li, B., Xue, W., Yao, X., Chen, Y., and Zhu, F. (2017) Differentiating physicochemical properties between addictive and nonaddictive ADHD drugs revealed by molecular dynamics simulation studies. *ACS Chem. Neurosci. 8*, 1416−1428.
(92) Xue, W., Wang, P., Li, B., Li, Y., Xu, X., Yang, F., Yao, X., Chen, Y. Z., Xu, F., and Zhu, F. (2016) Identification of the inhibitory mechanism of FDA approved selective serotonin reuptake inhibitors: an insight from molecular dynamics simulation study. *Phys. Chem. Chem. Phys. 18*, 3260−3271.
(93) *PyMOL Molecular Graphics System version 1.3*, Schrödinger, LLC.
(94) Massova, I., and Kollman, P. A. (2000) Combined molecular mechanical and continuum solvent approach (MM-PBSA/GBSA) to predict ligand binding. *Perspect. Drug Discovery Des. 18*, 113−135.
(95) Tippmann, S. (2014) Programming tools: adventures with R. *Nature 517*, 109−110.
(96) Letunic, I., and Bork, P. (2016) Interactive tree of life (iTOL) v3: an online tool for the display and annotation of phylogenetic and other trees. *Nucleic Acids Res. 44*, W242−245.
(97) Somoza, J. R., Skene, R. J., Katz, B. A., Mol, C., Ho, J. D., Jennings, A. J., Luong, C., Arvai, A., Buggy, J. J., Chi, E., Tang, J.,

DOI: 10.1021/acschemneuro.8b00729
ACS Chem. Neurosci. 2019, 10, 2467−2480

Sang, B. C., Verner, E., Wynands, R., Leahy, E. M., Dougan, D. R., Snell, G., Navre, M., Knuth, M. W., Swanson, R. V., McRee, D. E., and Tari, L. W. (2004) Structural snapshots of human HDAC8 provide insights into the class I histone deacetylases. *Structure 12*, 1325−1334.
(98) Decroos, C., Bowman, C. M., Moser, J. A., Christianson, K. E., Deardorff, M. A., and Christianson, D. W. (2014) Compromised structure and function of HDAC8 mutants identified in Cornelia de Lange Syndrome spectrum disorders. *ACS Chem. Biol. 9*, 2157−2164.
(99) Sun, H., Tian, S., Zhou, S., Li, Y., Li, D., Xu, L., Shen, M., Pan, P., and Hou, T. (2015) Revealing the favorable dissociation pathway of type II kinase inhibitors via enhanced sampling simulations and two-end-state calculations. *Sci. Rep. 5*, 8457.
(100) Hou, T., Wang, J., Li, Y., and Wang, W. (2011) Assessing the performance of the MM/PBSA and MM/GBSA methods. 1. The accuracy of binding free energy calculations based on molecular dynamics simulations. *J. Chem. Inf. Model. 51*, 69−82.
(101) Xu, L., Sun, H., Li, Y., Wang, J., and Hou, T. (2013) Assessing the performance of MM/PBSA and MM/GBSA methods. 3. The impact of force fields and ligand charge models. *J. Phys. Chem. B 117*, 8408−8421.
(102) Sun, H., Li, Y., Shen, M., Tian, S., Xu, L., Pan, P., Guan, Y., and Hou, T. (2014) Assessing the performance of MM/PBSA and MM/GBSA methods. 5. Improved docking performance using high solute dielectric constant MM/GBSA and MM/PBSA rescoring. *Phys. Chem. Chem. Phys. 16*, 22035−22045.
(103) Li, Y. H., Li, X. X., Hong, J. J., Wang, Y. X., Fu, J. B., Yang, H., Yu, C. Y., Li, F. C., Hu, J., Xue, W. W., Jiang, Y. Y., Chen, Y. Z., and Zhu, F. (2019) Clinical trials, progression-speed differentiating features and swiftness rule of the innovative targets of first-in-class drugs. *Briefings Bioinf.* Advance Access..
(104) Tang, J., Fu, J., Wang, Y., Li, B., Li, Y., Yang, Q., Cui, X., Hong, J., Li, X., Chen, Y., Xue, W., and Zhu, F. (2019) ANPELA: analysis and performance assessment of the label-free quantification workflow for metaproteomic studies. *Briefings Bioinf.* Advance Access.
.
(105) Ward, J. H. (1963) Hierarchical grouping to optimize an objective function. *J. Am. Stat. Assoc. 58*, 236−244.
(106) Rathi, P. C., Ludlow, R. F., Hall, R. J., Murray, C. W., Mortenson, P. N., and Verdonk, M. L. (2017) Predicting ″hot″ and ″warm″ spots for fragment binding. *J. Med. Chem. 60*, 4036−4046.
(107) Sinnokrot, M. O., and Sherrill, C. D. (2004) Substituent effects in $\pi-\pi$ interactions: sandwich and T-shaped configurations. *J. Am. Chem. Soc. 126*, 7690−7697.

DOI: 10.1021/acschemneuro.8b00729
ACS Chem. Neurosci. 2019, 10, 2467−2480